# Robust Multimodal Fusion of Transfer Learning Framework for Leukemia Cancer Detection and Classification using Biomedical Images

**Arwa Darwish Alzughaibi[1,*]**

[1]Applied College, Taibah University, Medina, Saudi Arabia

Email: azughaibi@taibahu.edu.sa

**Abstract**

Leukemia is a form of blood cancer that targets white blood cells (WBC) and stands as a major cause of mortality worldwide. During the center of human bones, leukaemia is presented and provides blood cell generation with leukocytes and WBC, and if some cell comes to be blasted, then it grows a fatal illness. For that reason, the analysis of leukaemia in its initial stages aids significantly in the treatment accompanied by saving the life. At present, leukemia analysis is done by visual assessment of biomedical images of blood cells, which is time-consuming, tedious, and wants to train specialists. Consequently, the lack of an early, automatic, and effectual leukemia recognition model is a major problem in hospitals. A few automated techniques like deep learning (DL) and Machine learning (ML) methodologies for leukemia cancer identification are presented that offer remarkable and effectual results. This study develops a Robust Multimodal Fusion of Transfer Learning Framework for Leukemia Cancer Detection and Classification (RMFTLF-LCDC) algorithm. The RMFTLF-LCDC system mostly suggests identifying and classifying the existence of leukemia cancer on biomedical imaging. At first, the RMFTLF-LCDC model applies image preprocessing using a kernel correlation filter (KCF) to eliminate the noise. For the feature extraction process, the multimodal fusion of CapsNet models, including RES-CapsNet, VGG-CapsNet, and GN-CapsNet are implemented to improve the representation of features by providing more accurate initial information to subsequent capsule layers. In addition, the recurrent spiking neural network with the spiking convolutional block attention module (RSNN-CBAM) technique is performed for the leukemia cancer detection process. At last, the improved Harris hawk optimization (IHHO) approach-based hyperparameter choice can be executed to improve the classification outcomes of the RSNN-CBAM system. The efficiency of the RMFTLF-LCDC method has been validated by comprehensive studies using the benchmark image dataset. The numerical result shows that the RMFTLF-LCDC method has better performance and scalability across other recent techniques.

**Keywords:** Leukemia Cancer Detection; Multimodal Fusion; Improved Harris Hawk Optimization; Biomedical Images; CapsNet

## 1. Introduction

The most significant portion of the human body is blood as it retains one life. It carries out numerous vital functions like transferring carbon dioxide, oxygen, minerals, and so on to the complete body to preserve metabolic rate [1]. Blood contains three major parts Platelets, WBC, and RBC. An inadequate quantity of blood might affect the metabolism significantly, which is life threatening when initial treatment is not taken. The general blood illness is Leukemia. It is a general kind of cancer in children [2]. Each cancer starts in cells of the blood, and leukemia represents cancer that starts in cells of the blood. Generally, cells develop and increase to grow new cells as the body requires them. After cells become older, they expire and new cells appear. Occasionally, this loop does not work properly. During cancer, new cells are made if the body does not require them, and aged cells must not expire once they can [3]. Leukemia is a cancer that includes the blood-producing tissues of the spleen, bone marrow, and lymph nodes [4]. One of the general categories is acute myelogenous leukemia (AML) and acute lymphocytic leukemia (ALL) which affect adults and children, correspondingly. ALL affect the WBC. This result makes a preventable variation count on the WBCs [5]. ALL takes place in children between the ages of 3 and 7, and closely



DOI: https://doi.org/10.54216/FPA.170230
Received: February 27, 2024 Revised: May 26, 2024 Accepted: October 30, 2024

two-thirds of identified registered cases have happened before the age of 6. According to the study of WHO, leukemia is the main cause of higher mortality rates from cancer [6]. Malignant WBCs additionally named lymphoblast go through the blood to other organs like the kidneys, brain, liver, and spleen, but they multiply to important body tissues. According to the microscopical images, a blood specialist in cell transplanting services could identify and distinguish several leukemia types [7]. When the slide is accurately marked, some types of leukemia are simpler to differentiate and recognize than others, but describing leukemia requires progressive technologies.

An initial identification of leukemia has consistently been a challenge to hematologist's investigators, and doctors [8]. Improvement of fever, lymph nodes, pallor, and weight loss are leukemia symptoms, and then they might be connected to another disease. Diagnosis of Leukemia is problematic in its initial phases because of the unimportant nature of the symptoms. During the past two decades, different investigations have accepted machine learning (ML) and computer-aided diagnosis (CAD) techniques in laboratory image examination, expecting to overwhelm the limitations of a later diagnosis of leukemia and outline its subsections [9]. ML is a renowned part of artificial intelligence (AI) with models and mathematic relationships, which was quickly presented to the domain of Medical study. The result of applying this method in clinical data processing is amazing, and they have achieved notable achievements in the diagnosis of disease [10]. Investigation specifies that, in medical image processing, ML techniques significantly help composite medical decision-making procedures by removing and then examining the features of these images.

This study develops a Robust Multimodal Fusion of Transfer Learning Framework for Leukemia Cancer Detection and Classification (RMFTLF-LCDC) algorithm. At first, the RMFTLF-LCDC model applies image preprocessing using a kernel correlation filter (KCF) to eliminate the noise. For the feature extraction process, the multimodal fusion of CapsNet models, including RES-CapsNet, VGG CapsNet, and GN-CapsNet are implemented to improve the representation of features by providing more accurate initial information to subsequent capsule layers. In addition, the recurrent spiking neural network with the spiking convolutional block attention module (RSNN-CBAM) technique is performed for the leukemia cancer recognition process. At last, the improved Harris hawk optimization (IHHO) approach-based hyperparameter choice can be executed to improve the classification outcomes of the RSNN-CBAM system. The efficiency of the RMFTLF-LCDC methodology has been validated by comprehensive studies utilizing the benchmark image database.

## 2. Review of Literature

Asar and Ragab [11] introduce a novel Falcon optimizer algorithm with a deep convolutional neural network (DCNN) for Leukemia detection and classification (FOADCNN-LDC) approach. Moreover, the proposed method uses the ShuffleNet-v2 system for the process of feature extraction. Additionally, the classification and detection of the process of leukemia are carried out by using the Convolutional Denoising Autoencoder (CDAE) algorithm. Ansari et al. [12] developed a deep learning (DL) algorithm with an adapted structure to detect critical leukemia with monocytes and lymphocyte images. This research proposed a new dataset comprising images of Acute Lymphocytic Leukemia (ALL) and Acute Myelogenous Leukemia (AML). The novel dataset is generated with the help of different specialists to assist the technical communities in their attempts to include ML models in clinical studies. Growing the scale of the dataset has been attained using a Generative Adversarial Network (GAN). In [13], a new DL approach depending on an enhanced ResNet-50 technique is progressed. This fine-tuning ResNet-50 technique incorporates different added modified fully connected (FC) layers, with dropout and dense layers. Furthermore, a five-fold cross-validation approach is utilized to improve the generalization models.

Elhassan et al. [14] presented a new algorithm by utilizing a hybrid approach depending on geometric transformation (GT) and deep convolution auto-encoder (DCAE), named the GT-DCAE WBC development method. Furthermore, to remove non-context-sensitive different features of WBC, this work improves a steady learning paradigm by including segmentation of WBC into DL. Jawahar et al. [15] proposed a Deep Dilated Residual CNN (DDRNet) algorithm. This method includes Deep Residual Dilated Blocks (DRDB) for quicker convergence. Traditional residual blocks are tactically located amongst layers. Global and Local Feature Enhancement Blocks (GLFEB) balanced poor assistances from shallowed layers for better feature normalization. In [16], an Optimal Attention-based DL with Segmentation for Automated Leukemia Detection and Classification (OADLS-ALDC) model has been presented. The OADLS-ALDC model mainly undertakes image preprocessing in dual stages: Dynamic Histogram Equalization (DHE) and Wiener Filter (WF). Simultaneously, the Watershed Segmentation algorithm has been used for segmenting the preprocessed images. Furthermore, the identification and recognition of leukemia occurs through the usage of the Attention Convolutional Recurrent Neural Network (ACRNN) method. Additionally, an RMSProp Optimizer has carried out the hyperparameter choice of the ACRNN technique.

Yenurkar et al. [17] implement a DL-based leukemia cancer classifier, especially a CNN pre-train technique, using microscopical cell images for detecting malignant cells. Utilizing preprocessing models like Region of Interest



DOI: https://doi.org/10.54216/FPA.170230
Received: February 27, 2024 Revised: May 26, 2024 Accepted: October 30, 2024

(RoI) extraction, picture scaling, feature extraction, and Improved Anisotropic Filtering (IAF), the blood cell image database was initially cleansed. Later healthy and leukemia-affected cells are assessed with different classification models and NNs, with optimum features recognized for enhancing the classifier performance. The authors [18] presented a lightweight DL-aided strong method dependent upon EfficientNetB3 with depth-wise separate convolutions to classify normal cells and critical lymphoblastic leukemia inside the WBC images database. The recommended lightweight EfficientNetB3 approach carries out lesser intelligent parameters to improve the efficiency and performance of leukemia classification.

## 3. Materials and Methods

In this manuscript, a novel RMFTLF-LCDC technique has been established. The RMFTLF-LCDC approach mostly suggests identifying and classifying the existence of leukemia cancer on biomedical imaging. To accomplish that, the RMFTLF-LCDC technique contains different kinds of stages involved as image preprocessing, multimodal fusion of TL, cancer detection using RSNN-CBAM, and IHHO-based parameter optimizer. Fig. 1 depicts the entire process of the RMFTLF-LCDC technique.

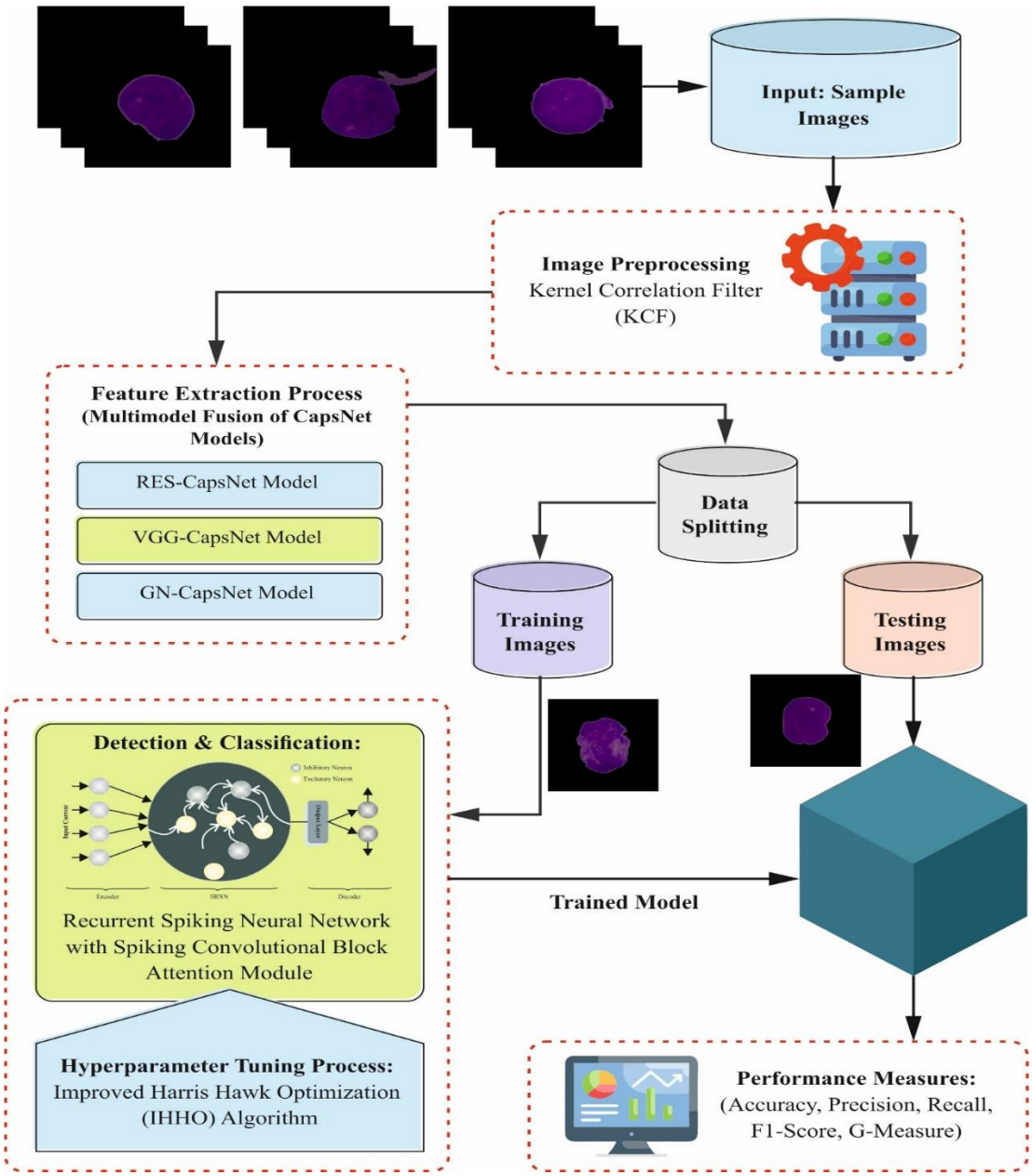


**Figure 1.** Overall process of RMFTLF-LCDC technique



DOI: https://doi.org/10.54216/FPA.170230
Received: February 27, 2024 Revised: May 26, 2024 Accepted: October 30, 2024

### 3.1. Stage I: Image Preprocessing

At first, the RMFTLF-LCDC model applies image preprocessing using KCF to eliminate the noise. The KCF model contains three phases such as training, recognition, and upgrading [19]. During the training phase, it proposes to improve the correlation filtering parameters utilizing the training feature-label pairs $\{x_i, y_i\}_{i=1}^{m}$. It plots the input $x$ to the original space $\varphi(x)$ with superior sizes and places the $\varphi(x)$ with the optimizer model. The kernel function $\kappa$ along with purpose of the optimizer are:

$$\kappa(x_i, x_j) = \langle \varphi(x_i), \varphi(x_j) \rangle. \tag{1}$$

$$\min_{w} \sum_{=1}^{m} w \left( y_j - \sum_{j=1}^{m} a_j \, \kappa(x_i, x_j) \right)^2 + \lambda \|w\|^2, \tag{2}$$

In which, $w$ is determined as:

$$w = \sum_{i=1}^{m} a_i \, \varphi(x_i). \tag{3}$$

The result of Eq. (2) is provided by deploying the circulant configuration to fast train and test,

$$\alpha = F^{-1} \left( \frac{F(Y)}{F^*(K_{xx}) + \lambda} \right), \tag{4}$$

Whereas $*$ implies the difficult conjugation, and $F$ and $F^{-1}$ demonstrate the inverse and Fourier transform, correspondingly, $K_{xx}$ stands for the kernel matrix.

During the recognition phase, it can calculate the possibility of original input $z$ derived from the target features.

$$Y' = F^{-1}\big(F * (K_{xz}) F(\alpha)\big). \tag{5}$$

During the upgrading phase, the reference feature $x$ and correlation filter parameters were estimated as:

$$x_t = z_t \times \eta + (1 - \eta) \times x_{t-1}, \tag{6}$$

$$\alpha_t = \alpha_{z_t} \times \eta + (1 - \eta) \times \alpha_{t-1}, \tag{7}$$

In which, $\eta$ represents the rate of learning.

### 3.2. Stage II: Multimodal Fusion of TL

For feature extraction process, the multimodal fusion of CapsNet models, including RES-CapsNet, VGG CapsNet, and GN-CapsNet. The basic CapsNet method input images were resized as 75x75 pixels to decrease the time of training [20]. The proposed method takes three arguments such as an input image, the count of routing iterations, and class counts. After preprocessed as in prior steps, served as the convolutional layer for extracting low-level features with kernel size is 9, strides is 1, and filters is 256. Then, these features are gathered into main capsules with filters of 8x32, kernel of 9x9, and stride of 1 for decreasing the size of model, each one signifying an aspect or part of an object. In the convolutional layer, every capsule resembles a capsule in the main layer of capsule. A routing-by-agreement technique is employed to increase learning capability and to take the relationship among dissimilar portions of an object. In a higher-level layer, each capsule delivers its output to capsules in the layer beyond depending upon the agreement (compatibility) among their outputs. The routing process consists of constantly upgrading the connection weights among capsules built on the match amongst their outputs. Therefore, dynamic routing forms the capsules in higher layer mainly concentrating on the most significant capsules in the below layer. The activation function of $ReLU$ represents a nonlinear function in deep neural networks (DNN), which is employed to decrease the size. The capsule network output is attained by evaluating the length of the capsule output vector in the highest layer. This length implies the likelihood that an assumed object or class exists in an input image. This study presents an enhanced CapsNet method, which includes significant pre-trained structures such as VGG16-CapsNet, RES-CapsNet, and GoogleNet(GN)-CapsNet. This incorporation intends to overcome the challenges in classification accuracy and spatial feature representation utilizing the deep features. Fig. 2 exemplifies the framework of CapsNet.



DOI: https://doi.org/10.54216/FPA.170230
Received: February 27, 2024 Revised: May 26, 2024 Accepted: October 30, 2024

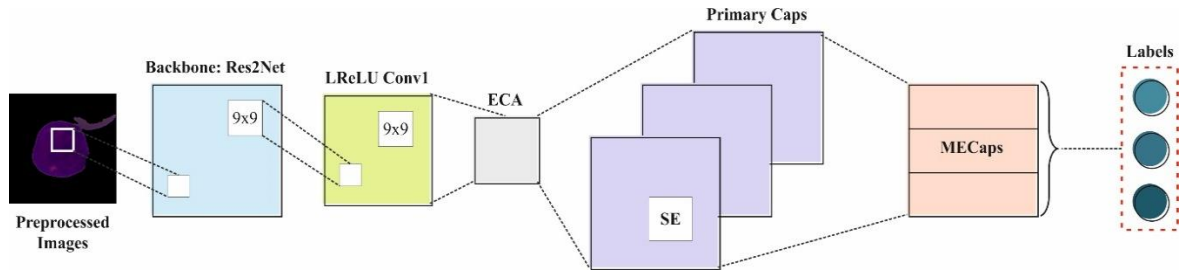


**Figure 2.** Framework of CapsNet

### 3.2.1. VGG16-CapsNet model

VGG16-CapsNet is a mixture of VGG16 method and CapsNet with great feature extraction, a decreased amount of model weight parameters, and diminished training time. VGG16 method contains 16 layers, which are highly trained on ImageNet and excerpt deep features, then served to main convolution layer of capsules with the stride is 2, filter size 8x32, and kernel size is 1. The Conv2D layer output is reformed to contest the preferred shape of the main capsule layer. The layer of reshaping is employed with the target shape [−1, 8]. The squash function is employed in the main capsule layer utilizing the layer of Lambda for normalizing the capsule vector length, certifying the range between 0 and 1. Then, batch normalization (BN) is used in the main capsule layer moment of 0.8, to retain the standard deviation output near to 1 and mean near to 0. The normalized output is compressed to serve a dense layer, which is named VGG16-Caps with 160 neurons. For every routing iteration of the dense layer, a sequence of processes is executed: dense layer and softmax with 160 neurons. Next, enlarge the resultant of the dense layer and exceed an output of multiplication to Leaky-ReLU layer. The last routing iteration output is passed over a dense layer with 32 neurons. Then, the model is forecasted utilizing the last output that is passed over a dense layer by the number of neurons equivalent to 21 class labels utilizing activation function of softmax to produce class probabilities. The frequent routing iterations improve the model's capability to achieve agreement amongst capsules and enhance the performance.

### 3.2.2. RES-CapsNet model

The RES-CapsNet method is a mixture of ResNetl52V2 method and CapsNet. The steps of preprocessing are repeated as similar to previous technique called VGG-CapsNet. Resized images with a 75x75 scale. Next, a pre-trained ResNetl52V2 technique is employed with 152 layers for extracting deep features. It can capture and learn intricate features from blood cell images, permitting the method to recognize the unique features of dissimilar cell types. Besides, ResNet employs skip connections to permit data to neglect numerous layers and avert the problem of vanished gradients in neural networks. The skip connection permits the method to acquire both lower and higher-level features and enable the vanishing gradient at the time of training. Then, these extracted features are to layers of capsule. Next, the similar procedure steps are related as similar as on preceding pre-train VGG16-CapsNet technique.

### 3.2.3. GN-CapsNet model

The GN-CapsNet technique is a mixture of the Google InceptionV3 and CapsNet for enhancing the efficacy of CapsNet. InceptionV3 is intended to capture features at numerous measures utilizing inception modules to permit the method and capture both high-level and fine-grained features. The inceptionV3 was an effective selection for examining images of blood cells and mining beneficial data. The preprocessing steps are similar to in preceding proposed methods with resized images 75x75 scale. Then, they were severed to main capsule layer. Do again the similar procedure steps as in prior proposed methods. The model is trained utilizing few parameters such as a loss is definite cross entropy and Adam optimizer. The hyperparameter is fine-tuned, such as decay of learning is 0.9, the rate of learning is 0.001, and it is normalized with a moment of 0.8.

### 3.3. Stage III: Cancer Detection using RSNN-CBAM

In addition, the RSNN-CBAM technique is performed for the leukemia cancer detection and classification process. The complete network of RSNN-CBAM involves a pooling layer, a layer of Spiking Convlstm with CBAM mechanisms, and fully connected (FC) layer [21]. Utilize pooling to diminish the data dimensionality and eliminate redundant data, employ Spiking Convlstm with CBAM mechanisms for extracting spatial and channel features, followed by guiding them to the classifier for classification.

**Spiking ConvLSTM**

ConvLSTM within SNN is presented, utilizing its capacity for space and time feature extraction to effectively handle time sequence information. Spiking ConvLSTM is equivalent to Ann ConvLSTM and additionally overwhelms the LSTM limitations in handling 3D data. Similarly, the conventional LSTM, the basic theory of



DOI: https://doi.org/10.54216/FPA.170230
Received: February 27, 2024 Revised: May 26, 2024 Accepted: October 30, 2024

spiking ConvLSTM rests in the state of a cell, $c_t$, and "gate" framework. The state of a cell can transfer related information in the sequence processing method completely. The "gate" architecture studies that data to forget or keep in training. Spiking ConvLSTM input was the 3D tensor, and the previous two sizes are spatial (Weight and Height). At the information on every time step $T$, Spiking ConvLSTM changes an operation of the connection part in LSTM by an operation of convolution that contains a structure of convolution in either input-to-state or state-wise changes, over the present input and the previous local neighbor state. Spiking ConvLSTM is better for treating dynamic spatial time-based patterns like gesture recognition with clean gesture movable paths but lacks protective fine-grained image details through higher-resolution pixels. More particularly, particular a collection of spiking inputs$x_1, x_2, , x_T$, the states and gates are considered below:

$$\begin{aligned} f_t &= \sigma_1\big(w_{f,\mathrm{h}} * h_{t-1} + w_{f,x} * x_t + b_f\big), \\ i_t &= \sigma_1\big(w_{i,h} * h_{t-1} + w_{i,x} * x_t + b_i\big), \\ g_t &= \sigma_2\big(w_{g,h} * h_{t-1} + w_{g,x} * x_t + b_g\big), \\ c_t &= f_t \odot c_{t-1} + i_t \odot g_t, \\ o_t &= \sigma_1\big(w_{o,h} * h_{t-1} + w_{o,x} * x_t + b_o\big), \\ h_t &= o_t \odot c_t, \end{aligned} \tag{8}$$

Whereas $\odot$ signifies the product of Hadamard,$*$ denotes the operation of convolution, and $\sigma_1$ and $\sigma_2$ are spike activation, which maps the membrane capacity of a neuron, for a spike when it surpasses the value of threshold correspondingly. Similarly,$b$, and $w$ represent related biases and weights, over the network, correspondingly. $x_t$ and $h_{t-1}$ individually corresponding in the spiking input during the present moment and the state of hidden at the earlier moment. The gate of forgetting, signified by $f_t$, adopts that data will be rejected. $i_t$ $th$ input gate that controls the data inputting the cell, contains other supplementary layers of input$g_t$, modified by other peak sigma activation. Lastly, the spiking ConvLSTM output has been designed depending on the cell state $c_t$ and output gate $o_t$.

**Spiking CBAM**

According to spiking ConvLSTM, the attention method is utilized in this study to enhance the forgetting gate.The spiking ConvLSTM using the CBAM part has been introduced to dynamically call historic data in time and space channels. The gate of forgetting in spiking ConvLSTM can be gained by splicing the pulse input toward the present moment and the state of hidden at the earlier moment after that gaining it throughout segmentation and convolution. After the CBAM element in RSNN-CBAM, the gate of forgetting can be employed as input, which would consecutively extract 1D channel attention mapping and the dual-dimension space attention mapping on the gate of forgetting, thus removing the spatial features and channel features from the gate of forgetting, and also, for time and space, the historic data within the channel has been fine-tuned. The complete attention method is summarized as:

$$\begin{aligned} f_t' &= M_c(f_t) \otimes f_t, \\ f_t'' &= M_s(f_t') \otimes f_t', \end{aligned} \tag{9}$$

Here $\otimes$ represents element-to-element multiplication. $M_c$ signifies the channel attention unit, and $M_s$ characterizes spatial attention unit. $Mc$ and $Ms$ successively perform channel and spatial extraction of features of the forgetting gate to produce channel attention unit $M_c(f_t)$ and spatial attention unit $M_s(f_t')$. $f_t''$ denotes the spiking output of CBAM. The subsequent defines every attention unit detail.

The channel attention element in Spiking CBAM utilizes pooling features of maximum and balance to create a 1D channel attention mapping of the forgetting gate over SNN-MLP. This channel attention can be considered as:

$$M_c(f_t) = \sigma\left(SMLP\big(AvgPool(f_t)\big) + SMLP\big(MaxPool(f_t)\big)\right) \tag{10}$$

Now $\sigma$ symbolizes spiking activation numbers, Maximum and Average pooling feature mapping sharing SNN-MLP weights.

The spatial attention part in Spiking CBAM employs pooling operations of average and maximum through the axis channel, executes the operation of convolution to it, and directs it within the spiking operation of activation to create the 2D spatial attention featured mapping of the forgetting gate. The spatial attention can be measured as:

$$M_s(f_t') = \sigma\big(f^{7\times7}([AvgPool(f_t'); MaxPool(f_t')])\big), \tag{11}$$



DOI: https://doi.org/10.54216/FPA.170230
Received: February 27, 2024 Revised: May 26, 2024 Accepted: October 30, 2024

Whereas $\sigma$ signifies spiking activation numbers, and $f^{7\times7}$ denotes the operation of convolution through a filter dimension of $7 \times 72$.

Over the above dual attention methods, the study gained the one-dimension channel attention mapping and dual-dimension spatial attention mapping of the forgetting gate, extracting the spatial and channel features of the gate of forgetting, and applied Spiking CBAM adaptively recollections historic data either temporal or spatial channels, and ablation visualizations and analysis are done to display the attention module efficiency.

### 3.4. Stage IV: IHHO-based Parameter Optimizer

Eventually, the IHHO approach-based hyperparameter choice can be executed to develop the classification outcomes of the RSNN-CBAM system. The HHOA is a heuristic optimizer method based on the Harris hawk performance approach [22]. The method understands the global optimization of the optimizer method by emulating raid-hunting tactics and Harris hawk group hunting behavior. The process of hunting can be separated into the exploration phase, the transformation from exploration to exploitation, along with exploitation phase.

**Exploration Phase**

During the exploration phase, the Harris hawk population entities arbitrarily dwelled anywhere, found and tracked prey based on their acute eyes, and searched for prey globally based on Eq. (12).

$$X(t+1) = \begin{cases} X_{rand}(t) - r_1|X_{rand}(t) - 2r_2X(t)|, & q \geq 0.5 \\ [X_{rabbit}(t) - X_m(t)] - r_3[lb + r_4(ub - lb)], & q < 0.5 \end{cases}, \quad (12)$$

Whereas $X(t)$ and $X(t+1)$ are the individual location vectors on the present and subsequent iterations, correspondingly; $t$ represents the number of iterations; $X_{rand}(t)$ signifies the arbitrarily chosen individual location; $X_{rabbit}(t)$ means the rabbit position; $r_1, r_2, r_3, r_4$, and $q$ are randomly generated values from the section of zero and one, $q$ can be utilized to choose the tactic to be implemented arbitrarily; $lb$ and $ub$ are the search space lower and upper limits; and $|X_{rand}(t) - 2r_2X(t)|$ presents a vector, which proceeds complete values component by component in a multidimensional space.

$$|X_{rand}(t) - 2r_2X(t)|$$
$$= \left(\left|X_{rand,1}(t) - 2r_2X_1(t)\right|, \left|X_{rand,2}(t) - 2r_2X_2(t)\right|, \cdots, \left|X_{rand,n}(t) - 2r_2X_n(t)\right|\right) \quad (13)$$

$X(t)$ denotes the individual average location, and the formulation is

$$X_m(t) = \frac{\sum_{k=1}^{m} X_k(t)}{M}, \quad (14)$$

whereas $X(t)$ represents the individual location $k$ in the population; $M$ signifies the dimension of the population.

**Transition from Exploration to Exploitation**

The Harris Hawk Optimization Algorithm (HHOA) transmutes among exploration and dissimilar exploitation performances depending upon the prey escaping energy. The escaped energy can be described as follows:

$$E = 2E_0\left(1 - \frac{t}{T}\right), \quad (15)$$

Whereas $E_0$ denotes the prey's primary energy that can be an arbitrarily produced number from the segment of $-1$ and 1, and it is spontaneously upgraded at every iteration; $t$ signifies the iteration counts; and $T$ denotes the maximal amount of iterations. $If\ |E| \geq 1$, it arrives in the exploration phase, and if $|E| < 1$, it arrives in the exploitation phase.

**Exploitation Stage**

According to the Harris hawk roundup tactic and prey escaping behavior, united with the escape energy of the prey $E$, the HHOA presents 4 tactics to imitate Harris hawk attacking behavior in the exploitation phase. The possibility of the target escapes can be represented by $r$. If $r \geq 0.5$, it represents that the prey is unsuccessful in escaping; if $r < 0.5$, the possibility of effective victim escape can be higher.

(1) if $0.5 \leq |E| < 1$ and $r \geq 0.5$, the location upgrade can be soft besiege:

$$X(t+1) = \Delta X(t) - E|IX_{rabbit}(t) - X(t)|, \quad (16)$$

whereas $\Delta X(t) = X_{rabbit}(t) - X(t)$ denotes the variance between the prey location and the present individual location; $J$ signifies a randomly generated number from the segment of zero and two.

(2) if $|E| < 0.5$ and $r \geq 0.5$, the location upgrade can be hard besiege:



DOI: https://doi.org/10.54216/FPA.170230
Received: February 27, 2024 Revised: May 26, 2024 Accepted: October 30, 2024

$$X(t+1) = X_{rabbit}(t) - E|\Delta X(t)|, \tag{17}$$

(3) if $0.5 \le |E| < 1$ and $r < 0.5$, the location upgrade can be soft besiege with increasing fast dives:

$$X(t+1) = \begin{cases} Y, f(Y) < f\big(X(t)\big) \\ Z, f(Z) < f\big(X(t)\big) \end{cases}, \tag{18}$$

$$Y = X_{rabbit}(t) - E|I^{X_{rabbit}}(t) - X(t)|, \tag{19}$$

$$Z = Y + S \times LF, \tag{20}$$

whereas $f()$denotes the fitness function; $D$ represents the problem size; $S$ can be a 1 x $D$ arbitrary vector; and Levy Flight ( LF ) signifies the Levy flight function, and its formulation can be

$$LF = 0.01 \times \frac{\mu \times \delta}{|\nu|^{\frac{1}{\beta}}}, \tag{21}$$

$$\delta = \left( \frac{\Gamma(1+\beta) \times \sin\left(\frac{\pi\beta}{2}\right)}{\Gamma\left(\frac{1+\beta}{2}\right) \times \beta \times 2^{\frac{\beta-1}{2}}} \right)^{\frac{1}{\beta}}, \tag{22}$$

whereas $\mu$ and $\nu$ are randomly generated values in $zero$ and $one$ $\beta$ is an arbitrary constant and is fixed to 1.5; and $\Gamma$ denotes the typical gamma function through the subsequent formulation:

$$\Gamma(x) = \int_0^{+\infty} e^{-t}\, t^{x-1} dt, \tag{23}$$

(4) if $|E| < 0.5$ and $r < 0.5$, the location upgrade is hard to besiege using gradual fast dives:

$$X(t+1) = \begin{cases} Y, f(Y) < f\big(X(t)\big) \\ Z, f(Z) < f\big(X(t)\big) \end{cases}, \tag{24}$$

$$Y = X_{rabbit}(t) - E|IX_{rabbit}(t) - X_m(t)|, \tag{25}$$

$$Z = Y + S \times LF, \tag{26}$$

Owing to certain failures in the HHO architecture, the searchability can be deficient, the process of search simply cascades into local optima, and the converging precision can be lower Thus, the HHOA can be enhanced by merging the dual adaptable weight tactic of the Dimension Learning-Based Hunting (DLH) search approach, in addition to location upgrade tactic united with the Dung Beetle Optimization method to increase its solution quality and converging speed.

**1. Double Adaptive Weights Approach**

The factor of inertia weighting plays a significant part in HHO that can be meticulously connected to the searchability of the method. In the method of creating the location, the dual adaptable weights $\omega_1$ and $\omega_2$ are utilized to upgrade the location. The weighted values are replaced with the process of iteration and altered to one another. The HHO exploration and exploitation capability is enhanced, and the converging precision and speed are enhanced. The particular formulations of $\omega_1$ and $\omega_2$ are as demonstrated:

$$\omega_1 = \left(1 - \frac{t}{T}\right)^{1-\tan\left(\pi\cdot(rand-0.5)\right)/T}, \tag{27}$$

$$\omega_2 = \left(2 - \frac{2t}{T}\right)^{1-\tan\left(\pi\cdot(rand-0.5)\right)/T}, \tag{28}$$

The method of iterative is separated into dual phases. In the exploration phase, Eq. (12) can be upgraded as shown:

$$X(t+1) = \begin{cases} \omega_1 X_{rand}(t) - r_1|X_{rand}(t) - 2r_2 X(t)|, & q \ge 0.5 \\ \omega_1[X_{rabbit}(t) - X_m(t)] - r_3[lb + r_4(ub - lb)] & q < 0.5 \end{cases}, \tag{29}$$

In the exploitation phase, Eqs. (16), (17), (19), and (25) are upgraded as follows:

$$X(t+1) = \omega_2 \Delta X(t) - E|IX_{rabbit}(t) - X(t)|, \tag{30}$$

$$X(t+1) = \omega_2 X_{rabbit}(t) - E|\Delta X(t)|, \tag{31}$$



DOI: https://doi.org/10.54216/FPA.170230
Received: February 27, 2024 Revised: May 26, 2024 Accepted: October 30, 2024

$$Y = \omega_2 X_{rabbit}(t) - E|I^{X_{rabbit}}(t) - X(t)|, \quad (32)$$

$$Y = \omega_2 X_{rabbit}(t) - E|I^{X_{rabbit}}(t) - X_m(t)|, \quad (33)$$

Afterward, creating the novel location, it's tested whether it cascades in the lower and upper limits of the search space population. Once it isn't fulfilled, it is modified based on Eq. (34) such that it drops into the possible solution space.

$$X(t+1) = \max(\min(X(t+1), ub), lb), \quad (34)$$

The IHHO approach produces a fitness function (FF) for achieving better classifier results. It resolves a positive integer to suggest a reliable result of candidate effectiveness. In this case, the diminished classifier error value is supposed that FF.

$$fitness(x_i) = ClassifierErrorRate(x_i)$$
$$= \frac{No.of\ misclassified\ instances}{Total\ no.of\ instances} * 100 \quad (35)$$

## 4. Experimental Result and Analysis

In this work, the empirical validation of the RMFTLF-LCDC model has been inspected under the Leukemia classification dataset [23]. The dataset contains 2000 images under two classes as represented in Table 1. Fig. 3 signifies the sample images.

**Table 1:** Details of Dataset

| **Class** | **No. of Images** |
|---|---|
| Normal Cell | 1000 |
| Leukemia Blast | 1000 |
| **Total Images** | **2000** |

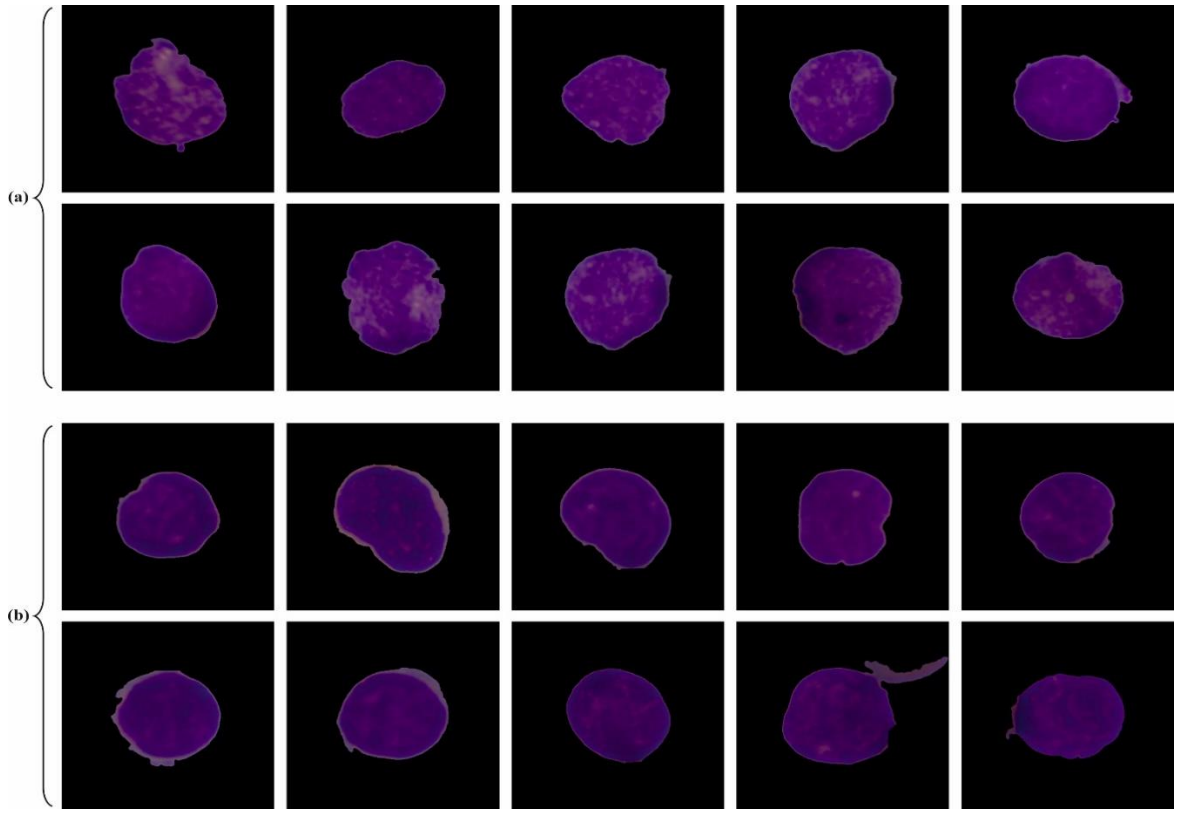


**Figure 3.** Sample Images



DOI: https://doi.org/10.54216/FPA.170230
Received: February 27, 2024 Revised: May 26, 2024 Accepted: October 30, 2024

Fig. 4 illustrates the confusion matrices generated by the RMFTLF-LCDC system under different epoch counts. The outcomes recognize that the RMFTLF-LCDC methodology has accurate identification and detection of all two-class labels.

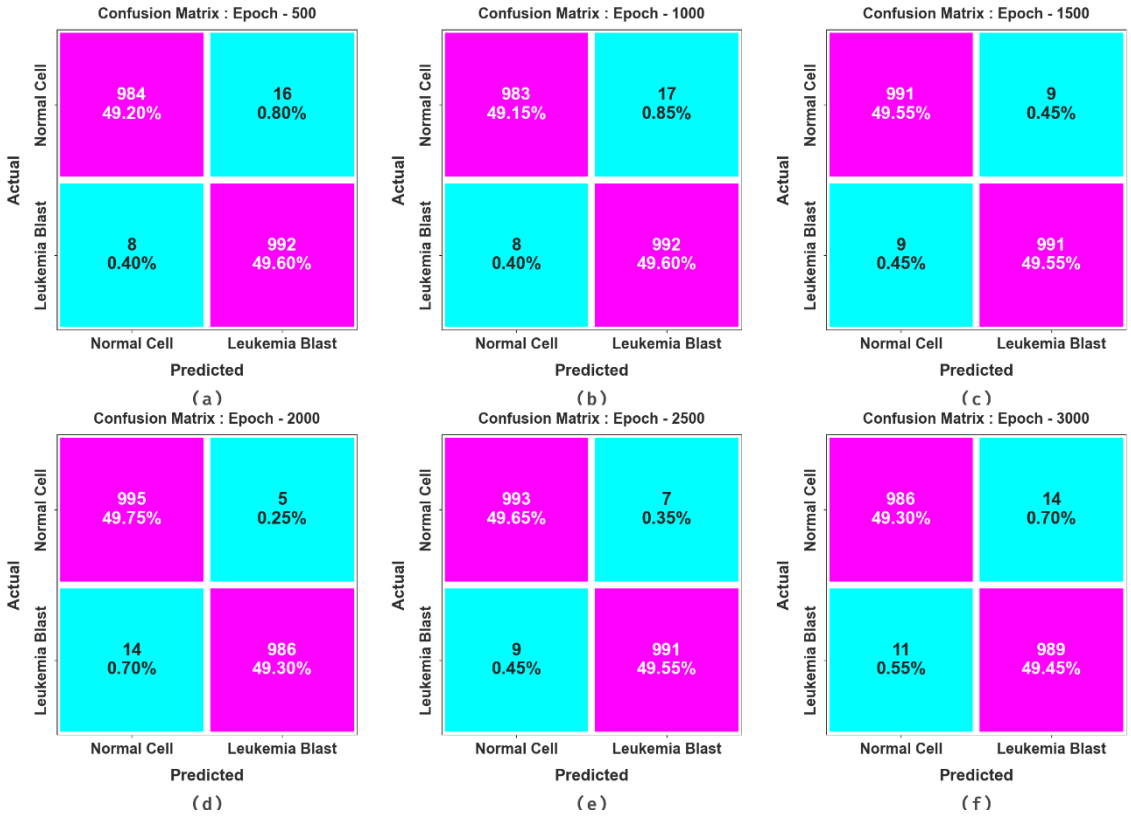


**Figure 4.** Confusion matrices of RMFTLF-LCDC technique (a-f) Epochs 500-3000

The Leukemia cancer detection outcomes of RMFTLF-LCDC approach are described on different epoch counts in Table 2 and Fig. 5. The table values showed that the RMFTLF-LCDC approach correctly identified all the samples. On 500 epoch counts, the RMFTLF-LCDC model offers an average $accu_y$ of 98.80%, $prec_n$ of 98.80%, $reca_l$ of 98.80%, $F1_{score}$ of 98.80%, and $G_{Measure}$ of 98.80%. Moreover, on 1000 epoch counts, the RMFTLF-LCDC method presents an average $accu_y$ of 98.75%, $prec_n$ of 98.75%, $reca_l$ of 98.75%, $F1_{score}$ of 98.75%, and $G_{Measure}$ of 98.75%. In the meantime, on 2000 epoch counts, the RMFTLF-LCDC system gives an average $accu_y$ of 99.05%, $prec_n$ of 99.05%, $reca_l$ of 99.05%, $F1_{score}$ of 99.05%, and $G_{Measure}$ of 99.05%. Additionally, on 2500 epoch counts, the RMFTLF-LCDC methodology produces an average $accu_y$ of 99.20%, $prec_n$ of 99.20%, $reca_l$ of 99.20%, $F1_{score}$ of 99.20%, and $G_{Measure}$ of 99.20%.

**Table 2:** Leukemia cancer detection outcome of RMFTLF-LCDC technique under distinct epochs

| Class | $Accu_y$ | $Prec_n$ | $Reca_l$ | $F1_{score}$ | $G_{Measure}$ |
|---|---|---|---|---|---|
| **Epoch - 500** | | | | | |
| Normal Cell | 98.40 | 99.19 | 98.40 | 98.80 | 98.80 |
| Leukemia Blast | 99.20 | 98.41 | 99.20 | 98.80 | 98.81 |
| **Average** | **98.80** | **98.80** | **98.80** | **98.80** | **98.80** |
| **Epoch - 1000** | | | | | |
| Normal Cell | 98.30 | 99.19 | 98.30 | 98.74 | 98.75 |
| Leukemia Blast | 99.20 | 98.32 | 99.20 | 98.76 | 98.76 |
| **Average** | **98.75** | **98.75** | **98.75** | **98.75** | **98.75** |
| **Epoch - 1500** | | | | | |
| Normal Cell | 99.10 | 99.10 | 99.10 | 99.10 | 99.10 |
| Leukemia Blast | 99.10 | 99.10 | 99.10 | 99.10 | 99.10 |
| **Average** | **99.10** | **99.10** | **99.10** | **99.10** | **99.10** |
| **Epoch - 2000** | | | | | |



DOI: https://doi.org/10.54216/FPA.170230
Received: February 27, 2024 Revised: May 26, 2024 Accepted: October 30, 2024

| | | | | | |
|---|---|---|---|---|---|
| Normal Cell | 99.50 | 98.61 | 99.50 | 99.05 | 99.06 |
| Leukemia Blast | 98.60 | 99.50 | 98.60 | 99.05 | 99.05 |
| **Average** | **99.05** | **99.05** | **99.05** | **99.05** | **99.05** |
| **Epoch - 2500** | | | | | |
| Normal Cell | 99.30 | 99.10 | 99.30 | 99.20 | 99.20 |
| Leukemia Blast | 99.10 | 99.30 | 99.10 | 99.20 | 99.20 |
| **Average** | **99.20** | **99.20** | **99.20** | **99.20** | **99.20** |
| **Epoch - 3000** | | | | | |
| Normal Cell | 98.60 | 98.90 | 98.60 | 98.75 | 98.75 |
| Leukemia Blast | 98.90 | 98.60 | 98.90 | 98.75 | 98.75 |
| **Average** | **98.75** | **98.75** | **98.75** | **98.75** | **98.75** |

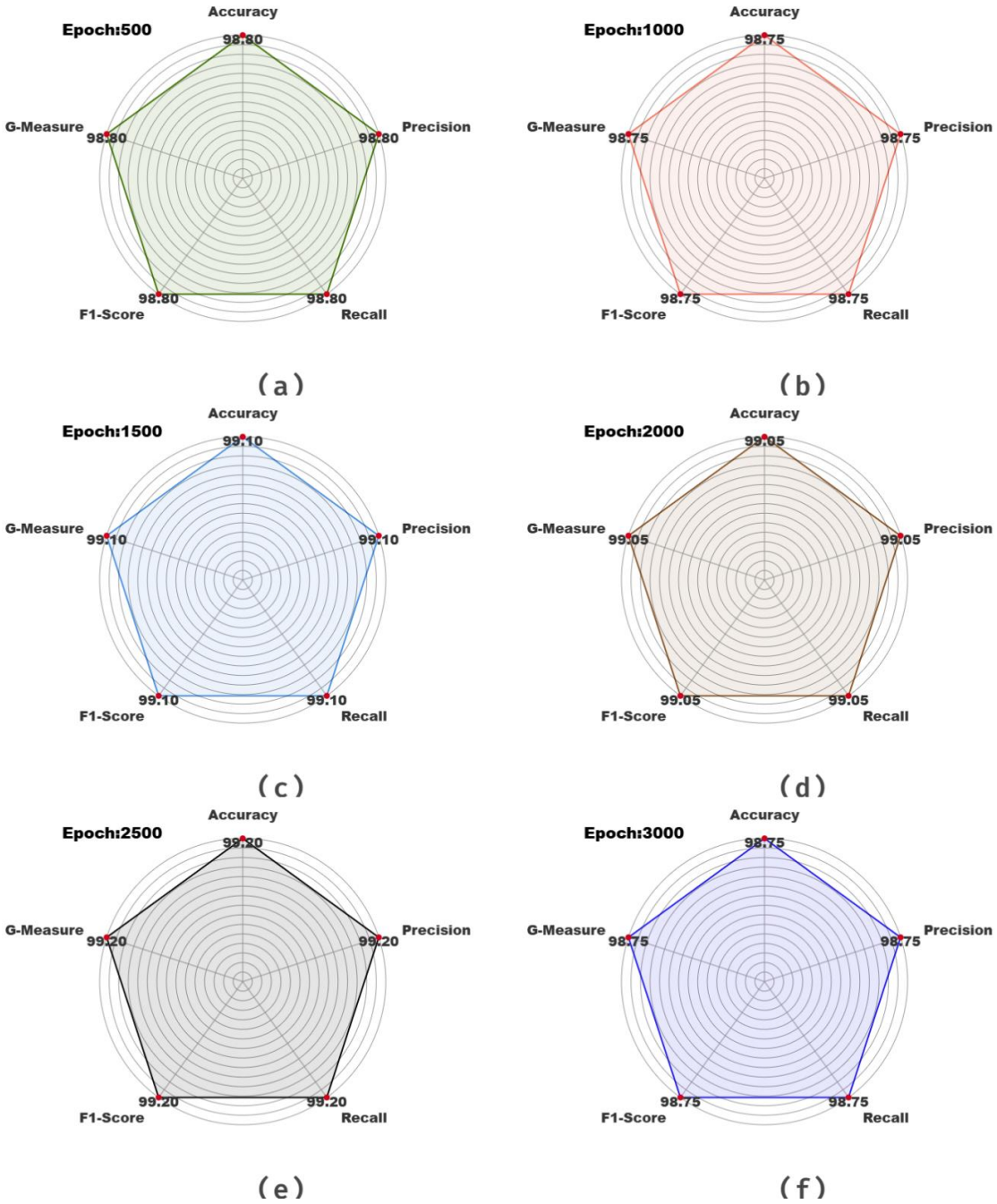


**Figure 5.** Average outcome of RMFTLF-LCDC model (a-f) Epochs 500-3000



DOI: https://doi.org/10.54216/FPA.170230
Received: February 27, 2024 Revised: May 26, 2024 Accepted: October 30, 2024

In Fig. 6, the training $accu_y$ (TRAAC) and validation $accu_y$ (VLAAC) outcomes of the RMFTLF-LCDC approach under various epoch counts can be represented. The $accu_y$values are calculated across an interval of 0-3000 epoch counts. The figure underlined that the TRAAC and VLAAC values show an increasing trend that informs the abilities of the RMFTLF-LCDC method with better performance throughout numerous iterations. Furthermore, the Training Accuracy (TRAAC) and Validation Accuracy (VLAAC) stay nearer above the epoch counts that designate less overfitting and display superior performance of the RMFTLF-LCDC algorithm, assuring steady prediction on unidentified samples.

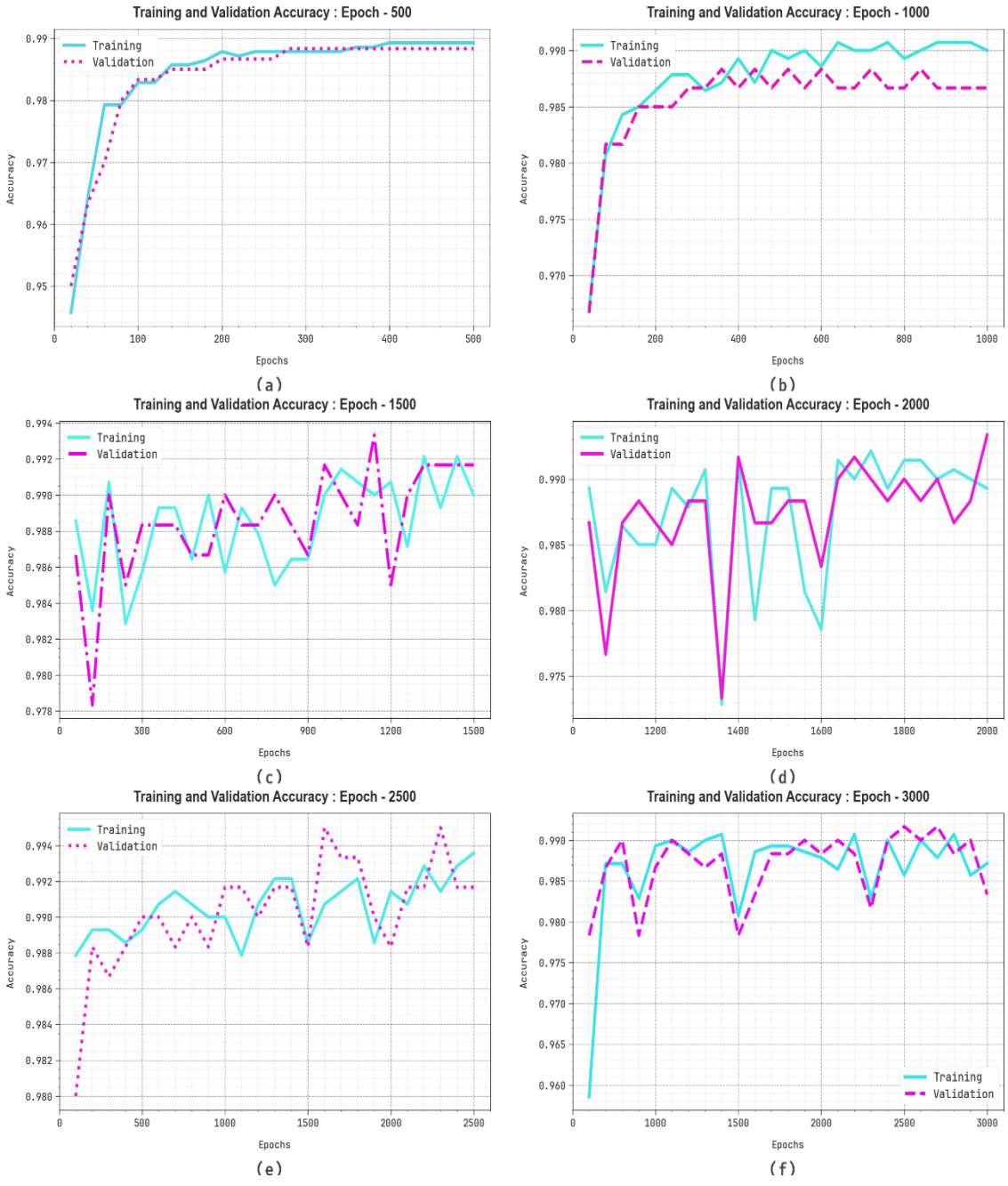


**Figure 6.** $Accu_y$ Curve of RMFTLF-LCDC model (a-f) Epochs 500-3000

In Fig. 7, the Traning Loss (TRALS) and Validation Loss (VLALS) graph of the RMFTLF-LCDC method under different epoch counts are determined. The loss values are calculated across an interval of 0-3000 epoch counts. It is signified that the TRALS and VLALS values point out a lessening trend, reporting the capabilities of the RMFTLF-LCDC method to balance a trade-off between data fitting and generalization. The incessant decrease in loss values also promises the improved performance of the RMFTLF-LCDC approach and tuning of the prediction results on time.



DOI: https://doi.org/10.54216/FPA.170230
Received: February 27, 2024 Revised: May 26, 2024 Accepted: October 30, 2024

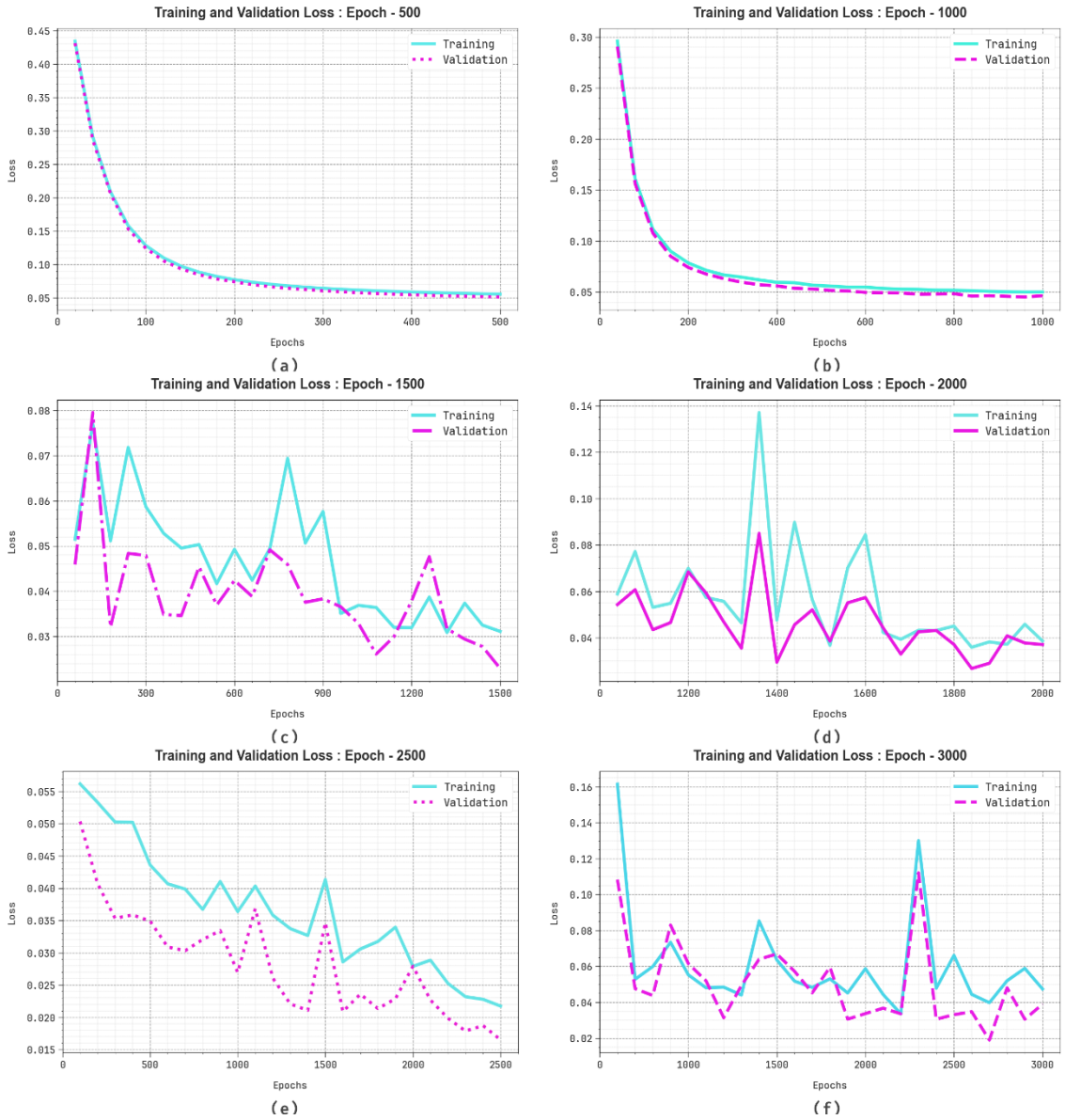


**Figure 7.** Loss curve of RMFTLF-LCDC model (a-f) Epochs 500-3000

In Fig. 8, the precision-recall (PR) examination study of the RMFTLF-LCDC approach on different epoch counts provides an understanding of its performance by plotting Precision against Recall for all class labels. The figure presents that the RMFTLF-LCDC technique incessantly achieves enhanced PR values through dissimilar classes, representing its capabilities to keep an important part of true positive predictions between every positive prediction (precision) however, additionally captures a larger amount of actual positives (recall). The continuous growth in PR results amongst every class label depicts the proficiency of the RMFTLF-LCDC method in the process of classification.

In Fig. 9, the ROC inspection of the RMFTLF-LCDC system under various epoch counts is investigated. The outcomes suggest that the RMFTLF-LCDC technique attains improved ROC results across every class, representing important capabilities of selecting the class labels. This consistent tendency of better ROC values across different class labels indicates the efficient performance of the RMFTLF-LCDC algorithm in predicting class labels, underlining the strong nature of the process of classification.



DOI: https://doi.org/10.54216/FPA.170230
Received: February 27, 2024 Revised: May 26, 2024 Accepted: October 30, 2024

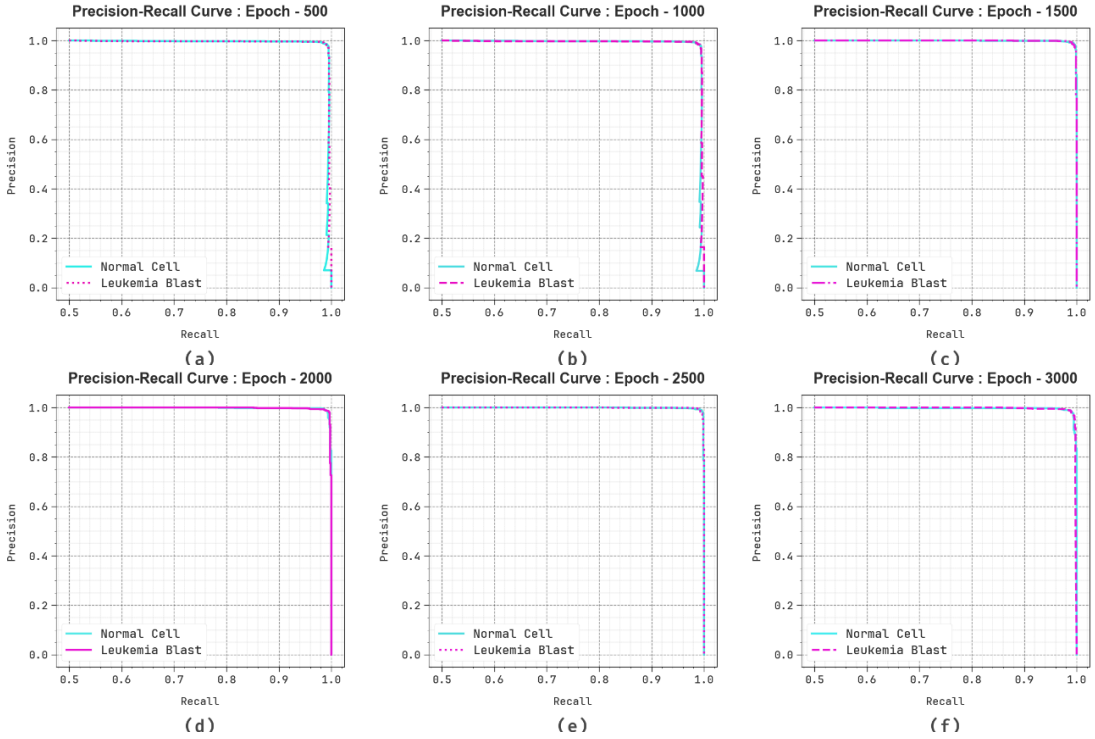


Figure 8**.** PR curve of RMFTLF-LCDC model (a-f) Epochs 500-3000

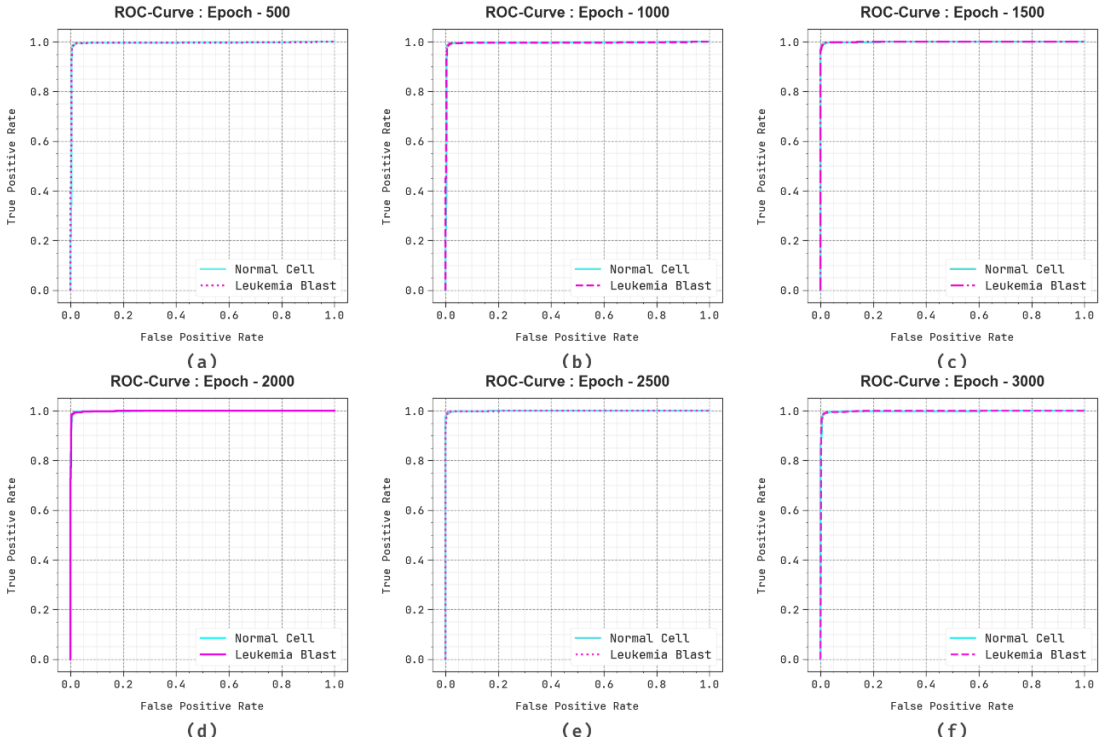


**Figure 9.** ROC curve of RMFTLF-LCDC model (a-f) Epochs 500-3000

The comparison study of RMFTLF-LCDC model with existing techniques is depicted in Table 3 and Fig. 10 [24-26]. The experimental result illustrated that the RMFTLF-LCDC method surpassed improved performances. According to $accu_y$, the RMFTLF-LCDC system has a greater $accu_y$ of 99.20% while the VGG16 + ECA, NasNetLarge + VGG19, VIT-CNN Ensemble, RF, SVM, ResNet50+Adaboost, and DenseNet121+Navive Bayes techniques have least $accu_y$ of 91.00%, 96.58%, 99.03%, 97.60%, 98.85%, 83.20%, and 89.72%, individually. Similarly, depends on $prec_n$, the RMFTLF-LCDC algorithm has better $prec_n$ of 99.20% while the VGG16 +



DOI: https://doi.org/10.54216/FPA.170230
Received: February 27, 2024 Revised: May 26, 2024 Accepted: October 30, 2024

ECA, NasNetLarge + VGG19, VIT-CNN Ensemble, RF, SVM, ResNet50+Adaboost, and DenseNet121+Navive Bayes systems have lower $prec_n$ of 93.12%, 93.41%, 90.85%, 98.20%, 99.00%, 93.70%, and 91.49%, correspondingly. Eventually, depends on $F1_{score}$, the RMFTLF-LCDC method has maximum $F1_{score}$ of 99.20% while the VGG16 + ECA, NasNetLarge + VGG19, VIT-CNN Ensemble, RF, SVM, ResNet50+Adaboost, and DenseNet121+Navive Bayes methodologies have minimum $F1_{score}$ of 89.94%, 91.13%, 91.96%, 97.60%, 98.80%, 88.40%, and 90.08%, correspondingly.

**Table 3:** Comparative analysis of RMFTLF-LCDC approach with existing methodologies

| **Methods** | $Accu_y$ | $Prec_n$ | $Reca_l$ | $F1_{score}$ |
|---|---|---|---|---|
| VGG16 + ECA module | 91.00 | 93.12 | 91.27 | 89.94 |
| NasNetLarge + VGG19 | 96.58 | 93.41 | 89.37 | 91.13 |
| VIT-CNN Ensemble Model | 99.03 | 90.85 | 91.73 | 91.96 |
| Random Forest Classifier | 97.60 | 98.20 | 97.60 | 97.60 |
| Support Vector Machine | 98.85 | 99.00 | 98.80 | 98.80 |
| ResNet50+Adaboost | 83.20 | 93.70 | 83.70 | 88.40 |
| DenseNet121+Navive Bayes | 89.72 | 91.49 | 89.80 | 90.08 |
| RMFTLF-LCDC | 99.20 | 99.20 | 99.20 | 99.20 |

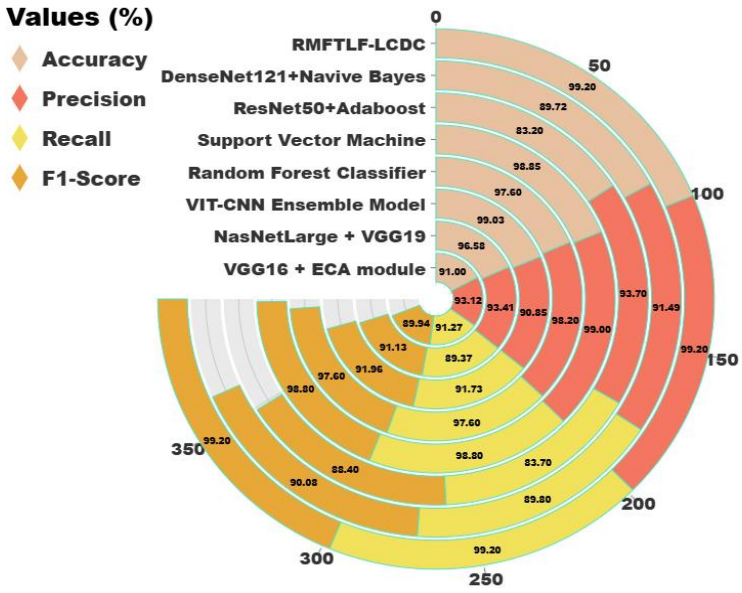


**Figure 10.** Comparative analysis of RMFTLF-LCDC approach with existing methodologies

In Table 4 and Fig. 11, the comparison results of the RMFTLF-LCDC approach are identified under computational time (CT). The outcomes represented that the RMFTLF-LCDC system acquires superior performance. According to CT, the RMFTLF-LCDC approach offers least CT of 10.94s while the VGG16+ECA, NasNetLarge+VGG19, VIT-CNN Ensemble, RF, SVM, ResNet50+Adaboost, and DenseNet121+Navive Bayes techniques achieve higher CT values of 18.80s, 20.21s, 15.26s, 16.14s, 21.81s, 20.97s, and 15.22s, respectively.



DOI: https://doi.org/10.54216/FPA.170230
Received: February 27, 2024 Revised: May 26, 2024 Accepted: October 30, 2024

**Table 4**: CT outcome of RMFTLF-LCDC approach with existing models

| **Methods** | **Computational Time (sec)** |
|---|---|
| VGG16 + ECA module | 18.80 |
| NasNetLarge + VGG19 | 20.21 |
| VIT-CNN Ensemble Model | 15.26 |
| Random Forest Classifier | 16.14 |
| Support Vector Machine | 21.81 |
| ResNet50+Adaboost | 20.97 |
| DenseNet121+Navive Bayes | 15.22 |
| RMFTLF-LCDC | 10.94 |

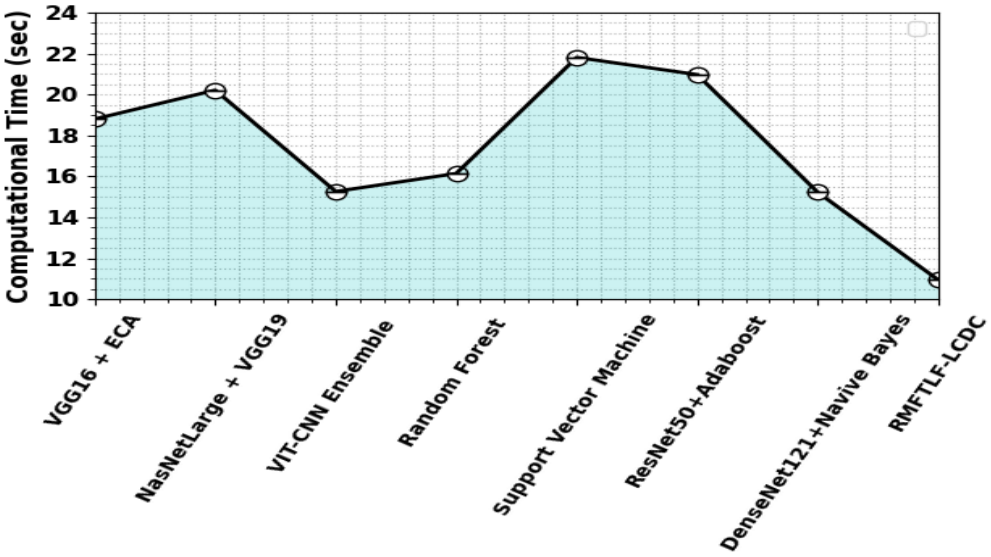


**Figure 11.** CT outcome of RMFTLF-LCDC approach with existing models

## 5. Conclusion

This paper introduces a newly developed RMFTLF-LCDC technique. The RMFTLF-LCDC approach mostly suggests identifying and classifying the presence of leukemia cancer on biomedical imaging. To accomplish that, the RMFTLF-LCDC technique contains different kinds of stages involved as image preprocessing, multimodal fusion of Transfer Learning (TL), cancer detection using RSNN-CBAM, and IHHO-based parameter optimizer. At first, the RMFTLF-LCDC model applies image preprocessing using KCF to eliminate the noise. For the feature extraction process, the multimodal fusion of CapsNet models, including RES-CapsNet, VGG-CapsNet, and GN-CapsNet are implemented to improve the representation of features by providing more accurate initial information to subsequent capsule layers. In addition, the RSNN-CBAM technique is performed for the leukemia cancer detection and classification process. Eventually, the IHHO approach-based hyperparameter choice can be executed to improve the classification outcomes of the RSNN-CBAM system. The efficiency of the RMFTLF-LCDC methodology has been validated by comprehensive studies using the benchmark image dataset. The numerical result shows that the RMFTLF-LCDC method has better performance and scalability across other recent techniques.

**Data Availability Statement:** The data that support the findings of this study are openly available in Kaggle repository at https://www.kaggle.com/datasets/andrewmvd/leukemia-classification, reference number [23].



DOI: https://doi.org/10.54216/FPA.170230
Received: February 27, 2024 Revised: May 26, 2024 Accepted: October 30, 2024

**References**


**[1]** Saeed, U., Kumar, K., Khuhro, M.A., Laghari, A.A., Shaikh, A.A. and Rai, A., DeepLeukNet—A CNN based microscopy adaptation model for acute lymphoblastic leukemia classification. Multimedia Tools and Applications, 83(7), pp.21019-21043, 2024.

**[2]** Elsayed, B., Elhadary, M., Elshoeibi, R.M., Elshoeibi, A.M., Badr, A., Metwally, O., ElSherif, R.A., Salem, M.E., Khadadah, F., Alshurafa, A. and Mudawi, D., Deep learning enhances acute lymphoblastic leukemia diagnosis and classification using bone marrow images. Frontiers in Oncology, 13, p.1330977, 2023.

**[3]** Baig, R., Rehman, A., Almuhaimeed, A., Alzahrani, A. and Rauf, H.T., Detecting malignant leukemia cells using microscopic blood smear images: a deep learning approach. Applied Sciences, 12(13), p.6317, 2022.

**[4]** Perveen, S., Alourani, A., Shahbaz, M., Ashraf, U. and Hamid, I., A framework for Early Detection of Acute Lymphoblastic Leukemia and its Subtypes from Peripheral Blood Smear Images Using Deep Ensemble Learning Technique. IEEE Access, 2024.

**[5]** Yadav, D.P., Kumar, D., Jalal, A.S., Kumar, A., Singh, K.U. and Shah, M.A., Morphological diagnosis of hematologic malignancy using feature fusion-based deep convolutional neural network. Scientific Reports, 13(1), p.16988, 2023.

**[6]** Sampathila, N., Chadaga, K., Goswami, N., Chadaga, R.P., Pandya, M., Prabhu, S., Bairy, M.G., Katta, S.S., Bhat, D. and Upadya, S.P., 2022, September. Customized deep learning classifier for detection of acute lymphoblastic leukemia using blood smear images. In Healthcare (Vol. 10, No. 10, p. 1812). MDPI.

**[7]** Islam, M.M., Rifat, H.R., Shahid, M.S.B., Akhter, A. and Uddin, M.A., Utilizing Deep Feature Fusion for Automatic Leukemia Classification: An Internet of Medical Things-Enabled Deep Learning Framework. Sensors (Basel, Switzerland), 24(13), 2024.

**[8]** Gondal, C.H.A., Irfan, M., Shafique, S., Bashir, M.S., Ahmed, M., Alshehri, O.M., Almasoudi, H.H., Alqhtani, S.M., Jalal, M.M., Altayar, M.A. and Alsharif, K.F., Automated Leukemia Screening and Sub-types Classification Using Deep Learning. Computer Systems Science & Engineering, 46(3), 2023.

**[9]** Sinha, R., Sinha, K.K., Patel, M., Gupta, S. and Priya, S., Detection of Leukemia Disease using Convolutional Neural Network. In 2024 5th International Conference on Image Processing and Capsule Networks (ICIPCN) (pp. 451-456). IEEE, 2024.

**[10]** Menagadevi, M., Nirmala, M., Thiyagarajan, D. and Rajkumar, R., Web-based Approach for Detection of Acute Lymphoblastic Leukemia From Microscopic Blood Cell Images Using Convolutional Neural Network, 2023.

**[11]** Asar, T.O. and Ragab, M., Leukemia detection and classification using computer-aided diagnosis system with falcon optimization algorithm and deep learning. Scientific Reports, 14(1), p.21755, 2024.

**[12]** Ansari, S., Navin, A.H., Sangar, A.B., Gharamaleki, J.V. and Danishvar, S., A customized efficient deep learning model for the diagnosis of acute leukemia cells based on lymphocyte and monocyte images. Electronics, 12(2), p.322, 2023.

**[13]** Alim, M.S., Bappon, S.D., Sabuj, S.M., Islam, M.J., Tarek, M.M., Azam, M.S. and Islam, M.M., Integrating convolutional neural networks for microscopic image analysis in acute lymphoblastic leukemia classification: A deep learning approach for enhanced diagnostic precision. Systems and Soft Computing, 6, p.200121, 2024.

**[14]** Elhassan, T.A., Mohd Rahim, M.S., Siti Zaiton, M.H., Swee, T.T., Alhaj, T.A., Ali, A. and Aljurf, M., Classification of atypical white blood cells in acute myeloid leukemia using a two-stage hybrid model based on deep convolutional autoencoder and deep convolutional neural network. Diagnostics, 13(2), p.196, 2023.

**[15]** Jawahar, M., Anbarasi, L.J., Narayanan, S. and Gandomi, A.H., An attention-based deep learning for acute lymphoblastic leukemia classification. Scientific Reports, 14(1), p.17447, 2024.

**[16]** Vinurajan, I., Optimal Attention based Deep Learning with Segmentation Approach for Automated Leukemia Detection and Classification. Power System Technology, 47(2), 2023.

**[17]** Yenurkar, G.K., Mal, S., Thakur, N., Dhomne, S., Dhurve, M., Patel, M., Kulmeti, K. and Dhurve, H., DeepLeuk: a convolutional neural network pre-trained model for microscopic cell images-Based leukemia Cancer analysis. Multimedia Tools and Applications, pp.1-34, 2024.

**[18]** Batool, A. and Byun, Y.C., 2023. Lightweight EfficientNetB3 model based on depthwise separable convolutions for enhancing classification of leukemia white blood cell images. IEEE access, 11, pp.37203-37215, 2023.

**[19]** Yue, W., Xu, F. and Yang, J., Tracking-by-Detection Algorithm for Underwater Target Based on Improved Multi-Kernel Correlation Filter. Remote Sensing, 16(2), p.323, 2024.




DOI: https://doi.org/10.54216/FPA.170230
Received: February 27, 2024 Revised: May 26, 2024 Accepted: October 30, 2024

**[20]** Aydin Atasoy, N. and Faris Abdulla Al Rahhawi, A., Examining the classification performance of pre-trained capsule networks on imbalanced bone marrow cell dataset. International Journal of Imaging Systems and Technology, 34(3), p.e23067, 2024.

**[21]** Xu, Q., Gao, Y., Shen, J., Li, Y., Ran, X., Tang, H. and Pan, G., Enhancing adaptive history reserving by spiking convolutional block attention module in recurrent neural networks. Advances in Neural Information Processing Systems, 36, 2024.

**[22]** Tang, C., Li, W., Han, T., Yu, L. and Cui, T., Multi-Strategy Improved Harris Hawk Optimization Algorithm and Its Application in Path Planning. Biomimetics, 9(9), p.552, 2024.

**[23]** https://www.kaggle.com/datasets/andrewmvd/leukemia-classification

**[24]** Saeed, A., Shoukat, S., Shehzad, K., Ahmad, I., Eshmawi, A.A., Amin, A.H. and Tag-Eldin, E., A deep learning-based approach for the diagnosis of acute lymphoblastic leukemia. Electronics, 11(19), p.3168, 2022.

**[25]** More, P. and Sugandhi, R., Automated and enhanced leucocyte detection and classification for leukemia detection using multi-class SVM classifier. Engineering Proceedings, 37(1), p.36, 2023.

**[26]** Sulaiman, A., Kaur, S., Gupta, S., Alshahrani, H., Reshan, M.S.A., Alyami, S. and Shaikh, A., ResRandSVM: Hybrid approach for acute lymphocytic leukemia classification in blood smear images. Diagnostics, 13(12), p.2121, 2023.

**[27]** Smarandache, F., Neutrosophic set a generalization of the intuitionistic fuzzy sets. Inter. J. Pure Appl. Math., 24, 287 – 297, 2005.

**[28]** Salama, A. A., Smarandache, F., & Kroumov, V., Neutrosophic crisp Sets & Neutrosophic crisp Topological Spaces. Sets and Systems, 2(1), 25-30, 2014.

**[29]** Smarandache, F. & Pramanik, S. (Eds). (2016). New trends in neutrosophic theory and applications. Brussels: Pons Editions.

**[30]** Alhabib, R., The Neutrosophic Time Series, the Study of Its Linear Model, and test Significance of Its Coefficients. Albaath University Journal, Vol.42, 2020, (Arabic version).



DOI: https://doi.org/10.54216/FPA.170230
Received: February 27, 2024 Revised: May 26, 2024 Accepted: October 30, 2024